Biophysical Journal Volume 98 June 2010 3035–3043

Characterization of the Decaheme *c*-Type Cytochrome OmcA in Solution and on Hematite Surfaces by Small Angle X-Ray Scattering and Neutron Reflectometry

A. Johns,[†] L. Shi,[§] T. Droubay,[§] J. F. Ankner,[‡] and L. Liang[†*]

[†]Environmental Sciences Division and [‡]Neutron Scattering Sciences Division, Oak Ridge National Laboratory, Oak Ridge, Tennessee; and [§]Pacific Northwest National Laboratory, Richland, Washington

ABSTRACT The outer membrane protein OmcA is an 85 kDa decaheme *c*-type cytochrome located on the surface of the dissimilatory metal-reducing bacterium *Shewanella oneidensis* MR-1. It is assumed to mediate shuttling of electrons to extracellular acceptors that include solid metal oxides such as hematite (α-Fe_2O_3). No information is yet available concerning OmcA structure in physiologically relevant conditions such as aqueous environments. We purified OmcA and characterized its solution structure by small angle x-ray scattering (SAXS), and its interaction at the hematite-water interface by neutron reflectometry. SAXS showed that OmcA is a monomer that adopts a flat ellipsoidal shape with an overall dimension of $34 \times 90 \times 65$ Å^3. To our knowledge, we obtained the first direct evidence that OmcA undergoes a redox state-dependent conformational change in solution whereby reduction decreases the overall length of OmcA by ~7 Å (the maximum dimension was 96 Å for oxidized OmcA, and 89 Å for NADH and dithionite-reduced OmcA). OmcA was also found to physically interact with electron shuttle molecules such as flavin mononucleotide, resulting in the formation of high-molecular-weight assemblies. Neutron reflectometry showed that OmcA forms a well-defined monomolecular layer on hematite surfaces, where it assumes an orientation that maximizes its contact area with the mineral surface. These novel insights into the molecular structure of OmcA in solution, and its interaction with insoluble hematite and small organic ligands, demonstrate the fundamental structural bases underlying OmcA's role in mediating redox processes.

INTRODUCTION

Dissimilatory metal-reducing bacteria (DMRBs) can couple the oxidation of carbon sources or molecular hydrogen (H_2) with the reduction of oxidized metals such as iron [Fe(III)] and manganese [Mn(IV)] (hydr)oxides (1). They therefore play an important role in the environmental cycling of Fe, Mn, and other metals, as well as carbon and various nutrient elements. In addition, DMRBs can be used to degrade organic compounds, reductively sequester radionuclides and metal contaminants in sediments, and generate electricity via microbial fuel cells (2,3). Although they are abundant in subsurface environments, Fe(III)/Mn(IV) oxides are insoluble at neutral pH and in the absence of strong complexing ligands. Some DMRBs, such as the Gram-negative bacterium *Shewanella oneidensis* MR-1, have the ability to transfer electrons extracellularly and to use these solid oxides as terminal electron acceptors (4). The electron transfer pathway employed by *S. oneidensis* MR-1 for extracellular reduction of Fe(III) oxides incorporates multiple components (3), including the multiheme cytochromes MtrA, MtrB, MtrC, and OmcA, which have been postulated to transfer electrons to the surface of Fe(III) oxides directly and/or indirectly via electron shuttles (5).

For direct electron transfer to occur, binding of the outer membrane reductases on mineral surfaces is required (6). Electron tunneling spectroscopy studies of OmcA and MtrC immobilized on gold surfaces via covalent linking have shown significant differences in the current-voltage response of these proteins, which represent intrinsic electron transfer properties (7). Cyclic voltammetry studies have also demonstrated the ability of OmcA to bind on, and exchange, electrons with iron oxide surfaces (8). For the indirect mechanism, the reduction of insoluble electron acceptors by OmcA and MtrC involves extracellular flavins acting as electron-shuttling agents (9,10). In vitro kinetic analyses of insoluble hematite and goethite reduction by membrane fractions and purified proteins have shown that reduction rates are significantly enhanced in the presence of extracellular flavins (11).

Despite recent advances in understanding the roles of MtrC and OmcA in extracellular reduction of Fe(III) oxides, the mechanistic basis for the metal reductase activity of MtrC and OmcA remains unknown, as the molecular structure for MtrC or OmcA has not been determined (7). Searches for structural templates in the protein database (PDB) using the sequences of OmcA and MtrC have provided no significant matches (12). Thus, the tertiary structure of these cytochromes likely adopts a new, hitherto uncharacterized fold. A secondary structure prediction covers only 14% of the OmcA sequence (see Fig. S1 *A* in the Supporting Material). The 10 heme attachment sites are distributed between two five-heme clusters separated by a 197-residue region of unknown fold (Fig. S1 *B*).

Submitted November 30, 2009, and accepted for publication March 16, 2010.

*Correspondence: liangl@ornl.gov

Editor: William C. Wimley.

0006-3495/10/06/3035/9 $2.00

doi: 10.1016/j.bpj.2010.03.049

Previous studies have described the structures of several bacterial multiheme cytochromes, including the nine-heme cytochrome *c* from *Desulfovibrio desulfuricans* (13) and the hexadecaheme cytochrome HmcA from *D. vulgaris* Hildenborough (DvH) (14). A common characteristic of multiheme cytochromes is the organization of hemes in clusters. It has been suggested that the spatial arrangement of these heme clusters enhances electron transfer among different protein components (14). Direct interaction between soluble and membrane-associated cytochromes is typically mediated by electrostatic interactions, as indicated by the presence of both negatively and positively charged surface patches.

We hypothesize that changes in the redox state of the heme moieties or binding of ligands may induce detectable conformational changes in the protein. These proposed changes in solution, and upon interaction with ligands, can be resolved by small angle x-ray scattering (SAXS). Unlike x-ray crystallography, which captures the crystal structure at atomic resolution under static conditions, SAXS can quantify changes in molecular conformations (e.g., due to redox reactions or ligand binding) in solution with high accuracy (15). The structures of buried interfaces can be uniquely probed by neutron reflectometry (NR) at subnanometer resolution. Hydrogen differs significantly from its stable isotope deuterium in its neutron scattering characteristics, which makes NR particularly useful for characterizing biological-mineral interfaces (16). In this study, we determine for the first time (to our knowledge) the low-resolution structure of OmcA in solution by SAXS, and its arrangement at the hematite (α-Fe_2O_3)-water interface by NR. We also provide the first direct evidence of redox state-dependent conformational changes in OmcA and additional evidence of its modes of interaction with Fe(III)-nitrilotriacetic acid (NTA), flavin mononucleotide (FMN), and anthraquinone-2,6-disulfonate (AQDS), which were previously shown to be redox partners for OmcA (5,11,17). By elucidating the redox and ligand-binding effects on the configuration of these proteins in solution, as well as the direct interaction with mineral surfaces, the results presented here will assist future investigations of OmcA that are expected to resolve detailed structure-function relationships between the heme moieties in OmcA and various electron acceptors.

MATERIALS AND METHODS

Protein expression and purification

A posttranslational modification results in the covalent attachment of fatty acids to the amino-terminal Cys of OmcA and MtrC (18). This lipoprotein modification likely facilitates integration into the outer membrane in vivo, but hinders structural characterization and controlled binding studies. In a previous study (18), a construct lacking the N-terminal cysteine residue accommodating a posttranslational lipid modification was used to eliminate unspecific interactions of the lipid-binding site with the mineral surface. It was shown that the redox properties and metal reductase activities were not altered by deletion of the lipid-binding site (8). In the study presented here, cell culture and expression of OmcA were performed as previously described for MtrA (19). To isolate OmcA, the cell pellets were resuspended in ice-cold buffer A (20 mM HEPES, pH 7.8, 5 mM β-mercaptoethanol, 150 mM NaCl, and 0.05% (w/v) of CHAPS) to which protease inhibitor (Roche Diagnostic, Indianapolis, IN) was added according to the manufacturer's instructions. The cells were lysed by passage through a French press three times at 8000 lb/in^2. Unbroken cells and debris were removed by centrifugation at 15000 $\times$ *g*, 4°C, for 30 min. The supernatant was transferred to an ultracentrifugation tube and centrifuged at 150,000 $\times$ *g* for 1 h. The supernatant was loaded to a 1 $\times$ 5 cm column of Ni^{2+}-NTA Sepharose (GE-Healthcare, Piscataway, NJ) preequilibrated with buffer A. The column was washed with 25 mL of the following ice-cold buffers in sequential order: buffer B (buffer A + 10% glycerol), buffer C (buffer B + 10 mM imidazole), and buffer D (buffer B + 40 mM imidazole). Finally, it was eluted with 10 mL buffer E (buffer B + 250 mM imidazole).

The identity of OmcA was confirmed by Western blot analysis with anti-V5 antibody (Invitrogen, Carlsbad, CA). The fractions containing OmcA were pooled and concentrated with an Amicon Ultra centrifugal device from Millipore (Billerica, MA). The concentrated OmcA was loaded on a HiLoad 16/60 column of Superdex 200 and eluted with buffer F (20 mM Tris, pH 7.8, 150 mM NaCl, 0.01% (w/v) CHAPS) by means of an ÄKTAexplorer fast protein liquid chromatography system (GE Healthcare, Piscataway, NJ). The purity of isolated OmcA was confirmed by staining with GelCode stain reagent (Pierce, Rockford, IL) after sodium dodecyl sulfate-polyacrylamide gel electrophoresis. The protein concentration was measured with a bicinchoninic acid protein assay kit from Pierce. Reduction of FMN and AQDS by purified OmcA was carried out according to established procedures (17,20).

SAXS

Data collection

The SAXS data were collected at SIBYLS beamline 12.3.1 (Advanced Light Source, Lawrence Berkeley National Laboratory, Berkeley, California). The energy of the incident x-ray beam was 11.0 keV, which corresponds to a wavelength of 1.13 Å. The distance between the sample and a MarCCD 165 x-ray detector system was 1.5 m, which resulted in an accessible *q*-range range of 0.010–0.32 Å^{-1}. The scattering vector is defined as $q = 4\pi\sin\theta/\lambda$, where 2θ is the scattering angle and λ is the wavelength of the incident beam. Aliquots of soluble OmcA were dialyzed at 4°C into a buffer of 20 mM Tris/HCl (pH 7.8), 150 mM NaCl, 3 mM NaN_3, 1 mM TCEP/HCl, 1.6 mM CHAPS, and 5% (v/v) glycerol. A detergent concentration, well below the critical micellar concentration (~8 mM) of CHAPS, was maintained to prevent formation of detergent micelles. Scattering profiles from a buffer before and after addition of CHAPS were compared to verify the absence of scattering from micelles. Reduced samples were prepared in an anaerobic glove box immediately before data were collected. OmcA was reduced by the addition of a 30-fold molar excess of either NADH or sodium dithionite. The change in the redox state was verified by measuring the absorption of β and α peaks at 523 and 552 nm, respectively. Protein samples for the ligand interaction studies were dialyzed into three separate buffer solutions, each containing a 24- to 40-fold molar excess of one of the following ligands: 3 mM Fe(III)-NTA, 5 mM FMN, and 5 mM AQDS.

Data were collected under anaerobic conditions by purging the sample environment with helium at 20°C and protein concentrations of 14.1, 7.0, 3.5, and 1.8 mg/mL. The sample volume for each run was 15 μL. Three successive frames with exposure times of 1, 10, and 1 s were recorded for each sample. The first and third frames were compared with each other to check for possible radiation damage in the protein. Background scattering from a buffer sample was recorded for equal lengths of time immediately before and after the protein sampling and subtracted from the scattering of the protein solution. Scattering intensities from the first two exposures were radially integrated and merged to obtain the final scattering profile, using short-exposure intensities for the low-*q* region and long-exposure intensities for the high-*q* region.

SAXS data reduction

Scattering profiles were processed with PRIMUS from the ATSAS 2.2 software package (21). The radius of gyration, R_g, was derived by the Guinier approximation $I(q) = I(0) \times \exp(-q^2 \times R_g^2/3)$ (22) as implemented in PRIMUS using scattering data in the low-q region ($q \times R_g < 1.3$). Extrapolation of the scattering intensities to the zero angle, $I(0)$, was performed to detect concentration-dependent protein interactions. Background-subtracted scattering data were subjected to indirect Fourier transformation using the program GNOM (23) to obtain electron pair distance distribution functions, $P(r)$. The maximum intraparticle distance, D_{max}, was determined by iterative fitting over a series of D_{max} values spaced by 0.5 Å, to maximize the total estimate as defined in GNOM.

Ab initio modeling was performed using the program GASBOR (24) without imposing symmetry constraints. To build a three-dimensional model of the protein in solution, GASBOR follows a chain-like spatial distribution of an exact number of dummy residues by minimizing the discrepancy between experimental data and scattering curves calculated from the model (25). A set of 20 independent models were aligned with SUPCOMB (26), and the best-fitting models were averaged using DAMAVER (27). The alignment of independent solutions gives an indication of the stability and consistency of ab initio modeling of SAXS data as defined by the normalized spatial discrepancy (NSD) (27), which measures the average distance between nearest-neighbor atoms in superimposed solutions. The average NSD for the GASBOR solutions was 1.1. Solutions with an NSD greater than two times the standard deviation were not included in the averaging process. The averaged models were converted into SITUS density maps (28) and visualized using the program VMD (29).

Iron oxide model interface

A novel hematite model interface was developed and optimized for use in NR studies. Silicon (Si) wafers with a diameter of 5 cm and a thickness of 5 mm were coated by pulsed laser deposition (PLD) with hematite (α-Fe_2O_3) thin films with thicknesses of 10–50 nm. The off-axis configuration of the PLD chamber minimizes deposition of droplets and helps ensure a more-uniform deposition for large substrates. Laser rastering from the KrF laser, target rotation, and substrate rotation were also utilized for uniform deposition. A chamber pressure of 10 mTorr molecular oxygen (O_2) was maintained during deposition with a flow of 3 sccm on the mass flow controller. After they were put into the PLD chamber, the Si substrates with native oxide were heated to 300°C in O_2 for 15 min before deposition to rid the surface of adventitious carbon. Typical deposition parameters for Fe_2O_3 thin films were 10 mTorr O_2, 300°C substrate temperature, and 5 Hz laser repetition rate. After growth was completed, the samples were cooled to room temperature in O_2 at a rate of ~25°C min^{-1}. The quality of the deposited iron oxide thin film was evaluated by scanning electron microscopy. No defects or surface inhomogeneities were observed (data not shown).

Neutron reflectivity

NR yields a layered profile perpendicular to an interface at subnanometer resolution. In this study, NR was used to reveal the spatial orientation of OmcA bound to the surface to gain structural information about the association of the protein at the mineral interface (16). The specularly reflected intensities were collected over a Q_Z range of $5.6 \times 10^{-3} - 0.3$ $Å^{-1}$. Reflectivity data could satisfactorily be fitted by a layer model, with thicknesses d_i, scattering length densities ρ_i, and protein volume fractions ϕ for the protein layer in contact with the solvent. The theoretical scattering length density for the hematite layer was calculated from its chemical composition (Fe_2O_3) and the specific density for hematite crystals (5.25 g/cm^3 (30)). Coherent neutron cross sections were obtained from the National Institute of Standards and Technology Center for Neutron Research (http://www.ncnr.nist.gov/resources/n-lengths/). The theoretical scattering length density for hematite is 7.19×10^{-6} $Å^{-2}$.

The wafers were cleaned in an ultraviolet cleaner before use. All data were collected at room temperature. To obtain baseline parameters of the iron oxide thin film, the reflectivity profiles of the hematite-coated silicon wafers were recorded in air. Adsorption of OmcA to the previously characterized hematite interface was performed in a solid-liquid sample cell. An aluminum ring was used to clamp the wafer to a stainless-steel sample holder equipped with a trough holding ~3 mL of liquid sealed by an O-ring. The trough was filled with solution through two filling ports, which were sealed with polytetrafluoroethylene stoppers. This assembly was mounted on the goniometer of the reflectometer and aligned along the axis of the incident neutron beam. Deuterium labeling of the solvent provided scattering contrast to the protein layer, which could readily be distinguished from the solvent and the iron oxide thin film. For NR experiments in the liquid cell setup, OmcA was dialyzed into a 99.9% D_2O buffer with 10 mM MOPS (3-(N-Morpholino)-propanesulfonic acid) and 10 mM KCl adjusted to pH 7.0 using NaOH. This pH corresponds to a pD of 7.4 due to a difference in the dissociation constants for H_2O and D_2O (31). The protein concentration of the solution injected into the liquid sample cell was 1.2×10^{-6} M or 0.1 mg/mL OmcA. The concentration, ionic strength, and pH were similar to conditions previously used for voltammetry and optical waveguide light-mode spectroscopy to determine the redox potentials and pH-dependent adsorption behavior of OmcA at mineral interfaces (8). After injection of the protein solution into the sample cell, the sample equilibrated for 1 h before NR data collection to allow sufficient time for self-assembly of the protein film on the hematite surface.

Data collection and reduction

NR data were collected with the liquids reflectometer (BL-4B) at the Spallation Neutron Source (SNS, Oak Ridge, TN). A polychromatic neutron beam (2.5 Å $< \lambda <$ 6.0 Å) with a pulse frequency of 60 Hz is reflected off the sample interface at a glancing angle θ. The intensity of the specular reflection $R(Q)$ is a function of the perpendicular component of the incoming wave vector $k_{iz} = Q/2 = (2\pi/\lambda)\ sin\theta$, and is measured as a function of the neutron wavelength λ at a sequence of fixed angles. The neutron wavelength λ is determined by means of the time-of-flight technique (32). The specular reflectivity $R(Q)$ may, in the Born approximation, be calculated from scattering-length density ρ_i in each layer i:

$$R(Q) = \frac{16\pi^2}{Q^2}\left|\widehat{\rho}(Q)\right|^2 \quad (1)$$

The function $\widehat{\rho}(Q)$ is the one-dimensional Fourier transform of $\rho(z)$ equivalent to:

$$\widehat{\rho}(Q) = \int_{-\infty}^{+\infty} e^{-iQz}\rho(z)dz \quad (2)$$

where $\rho(z)$ is the scattering-length density along the interface normal. This approximate representation highlights the relationship between specular reflectivity and neutron scattering density, which is less easily seen in the exact optical treatment we actually used to model the data.

The scattering length density in the protein layer is obtained from the volume fractions of protein and solvent:

$$\rho(z) = \phi_i\rho_P + (1 - \phi_i)\rho_S \quad (3)$$

where ρ_P and ρ_S correspond to the scattering-length densities of pure protein and solvent, respectively. The scattering-length density ρ of any given layer depends on its chemical composition:

$$\rho = \sum n_i b_i \quad (4)$$

where n_i is the number density and b_i is the scattering length of element i.

The intensity of the specular reflection was measured at seven incident angles θ (0.15°, 0.25°, 0.40°, 0.70°, 1.20°, 2.20°, and 3.30°) using

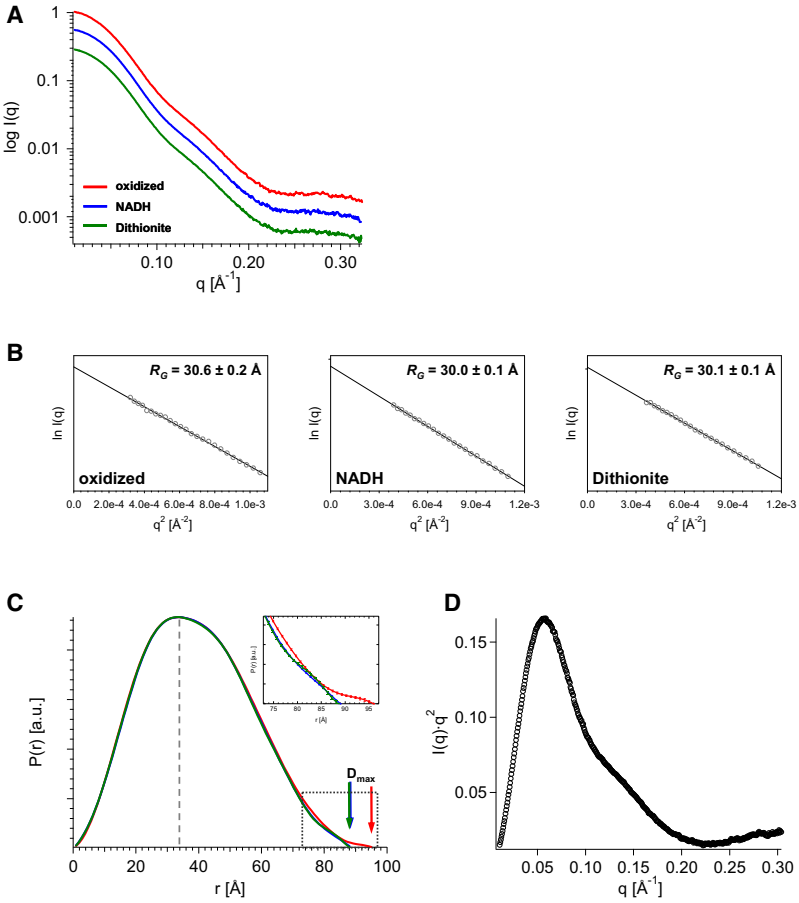

FIGURE 1 (*A*) X-ray solution scattering profiles for oxidized (*red*), NADH-reduced (*blue*), and dithionite-reduced (*green*) OmcA in solution. Plots are offset for clarity. (*B*) Guinier plots and radii of gyration obtained from the low-q region of the scattering profiles ($q \times R_g < 1.0$). (*C*) Electron pair distance distribution function $P(r)$ of oxidized OmcA (*red*), NADH-reduced (*blue*), and dithionite-reduced (*green*) OmcA. The maximum dimension D_{max} of oxidized OmcA was 96 Å; D_{max} for NADH- and dithionite-reduced OmcA was 89 Å. The dashed line indicates the most probable real-space length at 34 Å. The inset shows a magnification of the D_{max} region, including error bars. (*D*) Kratky-plot of raw SAXS data from oxidized OmcA shows that the protein is folded and contains no major unstructured regions.

a position-sensitive proportional counter, binned according to the neutron time-of-flight and merged into a single reflectivity profile using software provided by SNS. The thickness and interfacial roughness of each layer were derived from model-dependent fits to the experimental data. Data analysis was performed using fitting procedures employing the Parratt recursion formula (33) to calculate reflected intensities $R(Q)$ from a layer model of the scattering-length density profile perpendicular to the sample interface (Eqs. 1 and 2). Interfacial roughness was implemented by generating a discrete sequence of transitional steps following an error function profile (a Gaussian of full-width σ_i convoluted with a unit step function) (34,35). For data collected from the solid-liquid interface, the layer model used to fit the NR data from the hematite thin film was adapted to include additional parameters for the protein layer and a liquid subphase. Fitting of reflectivity data from the solid-liquid interface including the protein layer was constrained using the density, thickness, and roughness obtained from the fitting of the Fe_2O_3 thin film in air.

RESULTS AND DISCUSSION

Structural parameters for oxidized and reduced OmcA in solution

SAXS data were obtained for oxidized and reduced OmcA in solution (Fig. 1). A comparison of the scattering profiles (Fig. 1 *A*), Guinier plots (Fig. 1 *B*), and $I(0)/c$ acquired at four different concentrations (data not shown) shows no concentration dependence. This indicates a monodisperse distribution of OmcA in solution without aggregation. The molecular volume of OmcA as estimated from $I(0)$ and the Porod invariant (36) was 1.02×10^5 Å^3 ± 0.08×10^5 Å^3. Based on the amino acid sequence (37) and specific residue volumes (38), we calculated a theoretical molecular volume of 0.98×10^5 Å^3, which is in excellent agreement with the experimental value. This confirms that OmcA is a monomer in solution and likely adopts a compact conformation.

A direct visual comparison of the scattering curves between oxidized and reduced states of OmcA shows only minor differences (Fig. 1 *A*). However, the R_g for oxidized OmcA as obtained by the Guinier approximation was 30.6 ± 0.2 Å, whereas the R_g for NADH and dithionite-reduced OmcA were 30.0 ± 0.1 Å and 30.1 ± 0.1 Å, respectively (Fig. 1 *B*). Although the difference in R_g values is small, it indicates that a change in the redox state produces a conformational change in OmcA. The real-space R_g obtained from the $P(r)$ functions (Fig. 1 *C*) is consistent with the results obtained by the Guinier fits (Table 1). The pair distance distribution function showed a maximum near 34 Å for both oxidized and reduced OmcA. The most notable differences in the $P(r)$ were detected in the probabilities for large pair distances. The maximum dimension D_{max} as determined from the $P(r)$ was 96 Å for oxidized OmcA, and 89 Å for NADH and dithionite-reduced OmcA. These findings signify that a change in the redox state from an

TABLE 1 Changes in the radii of gyration R_g of OmcA between oxidized and reduced states, and effects of redox active ligands on association

Condition	Molar ratio of ligand/protein	Guinier R_g [Å]	R_g from $P(r)$	$I(0)/c$	Solution state
none	-	30.6 ± 0.2	30.6 ± 0.01	9.9	monodisperse
NADH	30	30.0 ± 0.1	30.3 ± 0.01	10.3	monodisperse
dithionite	30	30.1 ± 0.1	30.3 ± 0.01	10.6	monodisperse
Fe(III)-NTA	20	45.8 ± 0.4	-	14.1	oligomeric
FMN	40	46.9 ± 0.4	-	13.9	oligomeric
AQDS	40	40.4 ± 0.2	-	12.3	oligomeric

The apparent R_g is given for oligomeric samples. Limits for evaluation of R_g correspond to $q \times R_g < 1.0$.

oxidized to a reduced form decreases the overall protein length by ~7 Å.

Our SAXS results provide the first direct evidence, to our knowledge, that OmcA undergoes a redox-state-dependent conformational change in solution. It has been suggested that conformational changes could occur as a result of domain motions resulting in a spatial rearrangement upon binding to the hematite surface (6,8). Similar redox-dependent conformational changes were observed in a previous study upon reduction of a nine-heme cytochrome *c* from a different bacterial species, *D. desulfuricans* Essex (39). In that study, the spectroscopic and chromatographic data suggested that reduction by sodium dithionite alters the charge distribution in the macromolecule, which may result in the displacement of two rigid tetraheme cytochrome c_3-like domains. In this example, a flexible linker segment facilitates the interaction of the heme clusters with other cytochromes and electron acceptors. In our study, the primary structure of OmcA suggests a similar modular architecture with respect to the five-heme clusters. Thus, a Kratky plot was obtained to detect the presence of unfolded regions in OmcA (Fig. 1 *D*). The shape of the Kratky plot indicates that the protein is folded and contains no major unstructured regions in solution (15). Therefore, it is reasonable to assume that the observed conformational change in solution after reduction is caused by a redox-state-dependent charge redistribution in the heme groups, as opposed to an internal rearrangement of a large unstructured domain in the protein.

Ligand-induced conformational changes

OmcA was previously shown to interact with a number of small molecules in vitro. OmcA exhibits reductase activity toward Fe(III)-NTA and can be reduced by NADH (20). Likewise, OmcA was predicted to be able to transfer electrons to FMN (an endogenous electron shuttle produced by *S. oneidensis* MR-1) and AQDS (an artificial electron shuttle frequently used to enhance *S. oneidensis* MR-1's ability to reduce Fe(III) oxides) (5). However, no information was previously available about the mode of binding or changes in protein conformation associated with such interactions. The transfer of electrons between OmcA and an electron acceptor must involve docking of the ligand to a suitable binding site, minimizing the distance between hemes and allowing electron transfer to the ligand. On this basis, we hypothesized that the interaction with small redox-active ligands would induce sufficient changes in the conformation of OmcA to be observed by SAXS.

The presence of the small-molecule ligands Fe(III)-NTA, FMN, and AQDS resulted in an increase in the apparent size of OmcA (R_g) to 40.4–46.9 Å, from ~30 Å in the absence of these ligands (Table 1). Centrifugation of protein-ligand samples at 100,000 × *g* for 20 min did not produce precipitation of aggregated protein, suggesting that the ligands do not lead to unspecific aggregation or denaturation of OmcA. The average apparent molecular mass varied between 100 and 120 kDa, as estimated from extrapolation of the scattered intensity to zero angle $I(0)$ and comparison with a set of protein standards (40). This increase (compared to a molecular mass of 85 kDa in the absence of ligands) indicates that binding of these ligands results in the formation of a small fraction of oligomers within a limited size distribution in solution.

Although the exact composition and mode of association cannot be determined based on the available data, our findings suggest that binding of certain small, redox-active molecules alters OmcA's surface charge or hydrophobicity sufficiently to promote intermolecular association. A similar ligand-induced oligomerization behavior has been observed for other bacterial proteins (41) and is relevant for cell signaling mediated by membrane receptors (42). In the context of this study, such a mechanism may play a role in the transient formation of OmcA-MtrC complexes (20) and requires further investigation. Furthermore, the observed strong interaction between OmcA and Fe(III)-NTA is consistent with published results indicating that purified OmcA reduces Fe(III)-NTA by direct electron transfer (11,17). Binding of FMN and AQDS to OmcA may facilitate direct reduction of these ligands by OmcA, and indeed our experimental results showed that purified OmcA reduced FMN and AQDS in vitro (data not shown). The agreement between the in vitro study and published in vivo results showing that riboflavin is reduced by purified OmcA and MtrC, and AQDS is reduced by MtrC (11,43), confirms that such reductions are thermodynamically feasible (5). Reduction of FMN by OmcA also demonstrates the functional similarity between OmcA and bacterial assimilatory ferric

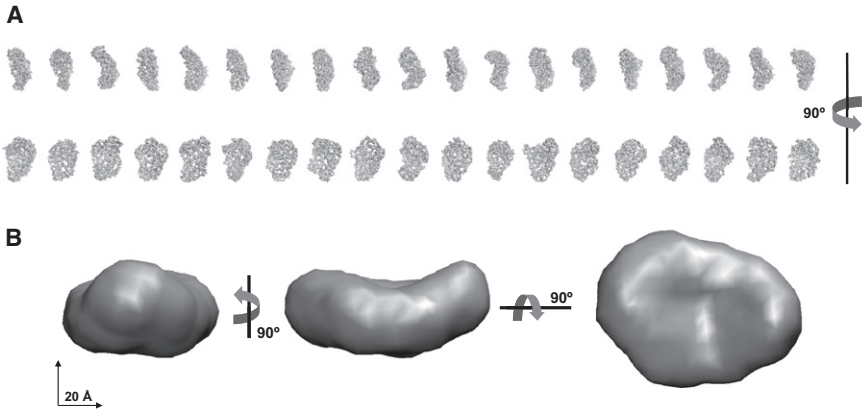

FIGURE 2 (*A*) Independent single models for oxidized OmcA obtained by the program GASBOR. (*B*) Low-resolution envelope shape derived from 19 ab initio reconstructions after averaging using the program DAMAVER.

reductases that use flavins as diffusible cofactors to reduce ferric iron (5,10,44).

Molecular envelope shape determined by SAXS

Low-resolution OmcA envelope shapes were obtained by ab initio shape reconstruction from experimental SAXS data using the program GASBOR. Single independent models with a similar quality of fit showed slight variations in the shape characteristics (Fig. 2 *A*). However, the average envelope shape represents spatial features common to all single models. The solution structure reveals a flat ellipsoidal shape with a length of ~90 Å, diameter of 65 Å, and thickness of ~34 Å (Fig. 2 *B*).

The molecular envelope shapes of OmcA in solution have not been previously determined. Available literature data are limited to OmcA that was covalently linked to a gold surface. The average size of OmcA in the resulting monolayer was ~80 Å as determined by scanning tunneling microscopy (7). Additional atomic force microscopy data suggested an estimated protein film thickness of 50–80 Å. However, this thickness estimate was determined by imaging the protein film and the gold surface in contact mode and in air (7). The lateral dimensions of a single OmcA molecule in solution obtained from ab initio shape reconstructions performed in this study were 65 × 90 Å, which is consistent with an average lateral dimension of ~80 Å. However, the molecular dimensions and the molecular model obtained by SAXS add significant detail to the very coarse size estimates reported in the literature.

Neutron reflectivity

Characterization of the hematite model interface

To characterize the thickness and overall roughness of the iron oxide-coated wafers, the NR profiles were first collected from bare films in air (Fig. 3). The iterative fitting of model parameters to the experimental reflectivity data yielded an actual scattering length density (SLD) of the deposited thin films of 6.60×10^{-6} Å^{-2}, which corresponds to 92% of the theoretical SLD for hematite. The iron oxide thin films also showed a nonuniform distribution of layer thickness across the wafer surface. Typically, the thickness of the hematite layer decreased from the center to the edge of the wafer, which may be an artifact of the laser-induced plasma plume used for deposition. Since the footprint of the neutron beam covers a surface area of ~12 cm^2, this thickness variation results in a significant smearing of the reflectivity profiles equivalent to an interfacial roughness of ~40 Å. The parameters obtained for the hematite layer were used as a baseline for fitting NR data collected in protein adsorption experiments.

Organization of OmcA at the hematite interface

The NR data were collected for adsorption of OmcA to the previously characterized hematite film in a liquid sample cell in which the incident neutron beam reflected off the

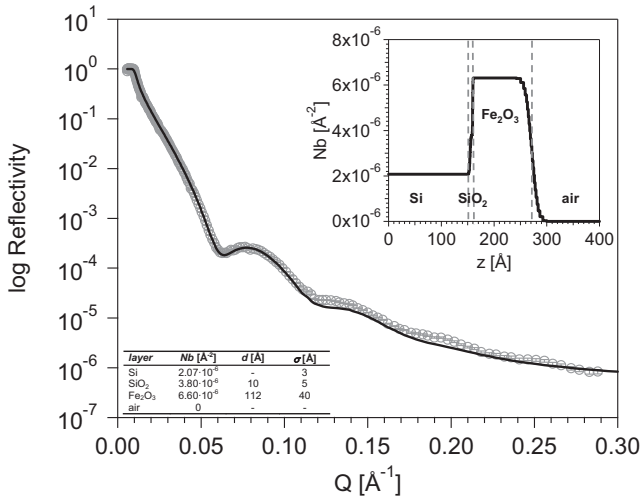

FIGURE 3 NR profile in air from a layer of Fe_2O_3 coated on a 5 cm Si wafer. The inset shows the scattering length density profile perpendicular to the interface. Parameters used to fit the experimental data are shown in the table on the bottom left. The density ρ of the Fe_2O_3 layer was obtained by fitting model parameters to the experimental data and corresponds to 92% of the theoretical ρ as calculated from the atomic composition and specific density of 5.25 g/cm^3.

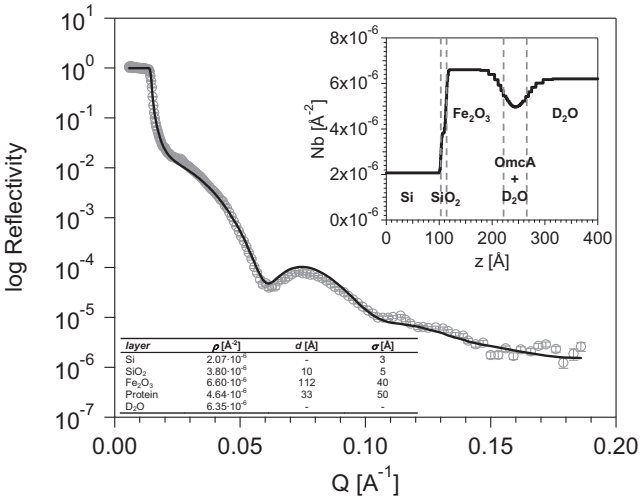

FIGURE 4 NR from a layer of OmcA adsorbed to the Fe_2O_3-coated 5 cm Si wafer shown in Fig. 3. The inset shows the corresponding scattering length density profile perpendicular to the surface. The parameters used to fit the experimental data are shown in the table on the bottom left. The thickness and scattering length density ρ of the protein were derived by fitting the multilayer model to the experimental data.

solid-liquid interface from within the Si substrate. Heavy water (D_2O) was used in the aqueous subphase to contrast-match the SLD of the hematite film. Results of the iterative parameter fitting are shown in Fig. 4. To accurately determine the volume fractions and packing densities of protein in the adsorbed layer, the SLDs and partial specific volumes of all components must be known. This calculation is based on the aggregate scattering density of the protein, which is a function of its atomic composition, the proportion of exchangeable hydrogen atoms it contains (because these protons will exchange with deuterons from the subphase), and its specific volume (Eqs. 3 and 4). The atomic composition of OmcA was calculated from its amino acid sequence (37), taking into account contributions from 10 heme moieties in the macromolecule. It was assumed that 80% of the labile hydrogen was exchanged, which is typical for proteins fully equilibrated in D_2O at neutral pH (45). The average partial specific volume of a protein is 0.73 cm^3/g (46). Accordingly, the scattering length density ρ_P of OmcA in D_2O was calculated to be 2.97×10^{-6} Å^{-2}. Under the given experimental conditions, the volume fraction ϕ of protein was 68% (Eq. 4), as determined from fitting model parameters to the experimental data. This ϕ-value yielded the adsorbed protein at the hematite interface at 164 ng/cm^2 or 1.9 pmol/cm^2, which is equivalent to ~83 nm^2 per OmcA molecule.

Binding of OmcA to hematite was previously reported to increase domain motions, as observed by fluorescence correlation spectroscopy (6). This suggests that OmcA possesses a significant amount of inherent flexibility. Given the irregularity of the mineral surface, this flexibility is critically important for maximizing the interaction of OmcA with the surface. In vivo, OmcA is anchored to the outer bacterial membrane via its N-terminal lipoprotein modification. This membrane attachment constrains the N-terminal region of the protein to cell membranes. Thus, the region interfacing with the mineral surface is most likely located closer to the C-terminus. Furthermore, the first heme-binding motif appears at a distance of >200 residues from the N-terminus (Fig. S1 *B*). Thus, we postulate that OmcA has a 200-residue N-terminal domain, which acts as a spacer that separates the redox-active heme clusters from the membrane surface. Changes in the redox state could affect the conformation of OmcA by altering the protonation states of amino acid residues in proximity to the heme moieties, resulting in a charge redistribution. OmcA binds to iron oxide surfaces, probably through its putative hematite binding motif, whose conserved sequence is Thr-Pro-Ser (47) (see also Fig. S1 *A*).

The molecular envelope as determined by SAXS shows that OmcA assumes a flat ellipsoidal shape in solution (Fig. 2). NR reveals a well-defined protein layer at the hematite-water interface with an average thickness of 33 Å. This value is consistent with the most probable real-space distance of 34 Å for OmcA in solution, as derived from the $P(r)$ function obtained by SAXS (Fig. 1 *C*). Furthermore, our ab initio envelope shape reconstruction indicates that OmcA adopts a flat particle shape (Fig. 2). Accordingly, the largest surface area of OmcA is in contact with the exposed mineral surface. On the basis of these results, we conclude that OmcA self-assembles at the hematite-water interface, forming a well-defined monomolecular layer with a surface coverage of 1.9 pmol/cm^2 under the conditions used in our experiments. The surface coverage of OmcA on hematite has been reported to vary between 1.2 and 2.6 pmol/cm^{-2} depending on the pH of the solution (6,8). However, no information about layer thickness and orientation was previously available. Our results suggest that OmcA adsorbs to hematite in an orientation that maximizes its contact area with the solid electron acceptor, as shown schematically in Fig. S2. In this manner, OmcA may transfer electrons to solid mineral surfaces directly, as suggested in the literature (8).

CONCLUSIONS

The multiheme *c*-type cytochrome OmcA from *S. oneidensis* MR-1 can serve as a terminal reductase to transfer electrons to an Fe(III)-containing mineral or other solid surfaces. Its activity is determined by changes in the redox state that can significantly affect its molecular conformation. We characterized redox-dependent and ligand-induced conformational changes of OmcA in solution by SAXS, and its association with a hematite surface by NR. In solution, the radii of gyration, R_g, obtained from the SAXS data show distinct differences between the oxidized and reduced forms. The maximum protein dimension, as determined from the pair distance distribution function, was 96 Å for oxidized OmcA and 89 Å for NADH and dithionite-reduced OmcA.

A change in redox state also appeared to affect protein length, slightly altering the overall molecular conformation in solution. Such a change may be caused by altered protonation states of amino acid residues in proximity to the heme moieties, resulting in a charge redistribution. However, the SAXS data also showed that OmcA lacks significant unstructured regions and adopts a compact, flattened conformation in solution, as evidenced by a structure model that revealed details of OmcA's molecular envelope, with dimensions of 90 Å × 65 Å × 34 Å. These findings add significant details to the very coarse size estimates previously reported in the literature (6).

In the presence of small redox-active ligands, OmcA formed oligomers in solution with a limited size distribution, suggesting that binding of the redox-active molecules alters the surface charge or hydrophobicity on OmcA and promotes intermolecular association (41). In the context of this study, such an association may be relevant to the transient formation of OmcA-MtrC complexes (20) and warrants further investigation. The finding that OmcA interacts with FMN supports the view that OmcA uses FMN as an electron shuttle for indirect reduction of iron oxides (9).

We postulate that the redox-active domain is spatially separated from the membrane-associated N-terminus, facilitating interaction with mineral surfaces. Upon contact with the mineral surface, OmcA may adjust its orientation to align the two five-heme clusters with the mineral surface to enable electron transfer. For the first time, to our knowledge, we were able to use NR to directly observe under physiologically relevant conditions in aqueous solution, that OmcA self-assembles into a monomolecular layer on a hematite surface, which is a prerequisite for direct electron transfer as proposed by others (8). The high-resolution data required for comprehensive interpretation of the structure-function relationships of OmcA's electron transfer mechanisms are not yet available. In particular, information about the orientation of heme clusters with respect to the mineral surface would help elucidate electron transfer pathways. Nonetheless, the structural information obtained here in solution with the use of SAXS and NR provides novel molecular-scale insights into a system that has important implications for biogeochemical metal cycling, contaminant biotransformation, and microbial fuel cell development.

SUPPORTING MATERIAL

Two additional figures are available at http://www.biophysj.org/biophysj/supplemental/S0006-3495(10)00415-7.

We thank Candice Halbert for excellent technical support at SNS beamline 4B.

This research was supported in part by the Laboratory Directed Research and Development Program of the Oak Ridge National Laboratory (ORNL). Additional funding was provided by the U.S. Department of Energy Office of Science, Biological, and Environmental Research. This work was performed at the following national scientific user facilities: the liquids reflectometer BL-4B at the Spallation Neutron Source (SNS) located at ORNL, the Environmental Molecular Sciences Laboratory at Pacific Northwest National Laboratory and the SIBYLS beamline at Lawrence Berkeley National Laboratory for SAXS experiments under contract No. DE-AC02-05CH11231. ORNL is managed by UT-Battelle, LLC, for the DOE under contract No. DE-AC05-00OR22725. Pacific Northwest National Laboratory is operated for the DOE by Battelle Memorial Institute under contract No. DE-AC05-76RLO1380.

REFERENCES

1. Nealson, K. H., and D. Saffarini. 1994. Iron and manganese in anaerobic respiration: environmental significance, physiology, and regulation. *Annu. Rev. Microbiol.* 48:311–343.
2. Lovley, D. R. 2008. The microbe electric: conversion of organic matter to electricity. *Curr. Opin. Biotechnol.* 19:564–571.
3. Weber, K. A., L. A. Achenbach, and J. D. Coates. 2006. Microorganisms pumping iron: anaerobic microbial iron oxidation and reduction. *Nat. Rev.* 4:752–764.
4. Myers, C. R., and K. H. Nealson. 1988. Bacterial manganese reduction and growth with manganese oxide as the sole electron acceptor. *Science.* 240:1319–1321.
5. Shi, L., D. J. Richardson, …, J. K. Fredrickson. 2009. The roles of outer membrane cytochromes of *Shewanella* and *Geobacter* in extracellular electron transfer. *Environ. Microbiol. Rep.* 1:220–227.
6. Xiong, Y., L. Shi, …, T. C. Squier. 2006. High-affinity binding and direct electron transfer to solid metals by the *Shewanella oneidensis* MR-1 outer membrane *c*-type cytochrome OmcA. *J. Am. Chem. Soc.* 128:13978–13979.
7. Wigginton, N. S., K. M. Rosso, …, M. F. Hochella. 2007. Electron tunneling properties of outer-membrane decaheme cytochromes from *Shewanella oneidensis*. *Geochim. Cosmochim. Acta.* 71:543–555.
8. Eggleston, C. M., J. Vörös, …, P. J. S. Colberg. 2008. Binding and direct electrochemistry of OmcA, an outer-membrane cytochrome from an iron reducing bacterium, with oxide electrodes: a candidate biofuel cell system. *Inorg. Chim. Acta.* 361:769–777.
9. von Canstein, H., J. Ogawa, …, J. R. Lloyd. 2008. Secretion of flavins by *Shewanella* species and their role in extracellular electron transfer. *Appl. Environ. Microbiol.* 74:615–623.
10. Marsili, E., D. B. Baron, …, D. R. Bond. 2008. *Shewanella* secretes flavins that mediate extracellular electron transfer. *Proc. Natl. Acad. Sci. USA.* 105:3968–3973.
11. Ross, D. E., S. L. Brantley, and M. Tien. 2009. Kinetic characterization of OmcA and MtrC, terminal reductases involved in respiratory electron transfer for dissimilatory iron reduction in *Shewanella oneidensis* MR-1. *Appl. Environ. Microbiol.* 75:5218–5226.
12. Altschul, S. F., W. Gish, …, D. J. Lipman. 1990. Basic local alignment search tool. *J. Mol. Biol.* 215:403–410.
13. Matias, P. M., R. Coelho, …, M. A. Carrondo. 1999. The primary and three-dimensional structures of a nine-haem cytochrome *c* from *Desulfovibrio desulfuricans* ATCC 27774 reveal a new member of the Hmc family. *Structure.* 7:119–130.
14. Matias, P. M., A. V. Coelho, …, M. A. Carrondo. 2002. Sulfate respiration in *Desulfovibrio vulgaris* Hildenborough. Structure of the 16-heme cytochrome c HmcA AT 2.5-A resolution and a view of its role in transmembrane electron transfer. *J. Biol. Chem.* 277:47907–47916.
15. Putnam, C. D., M. Hammel, …, J. A. Tainer. 2007. X-ray solution scattering (SAXS) combined with crystallography and computation: defining accurate macromolecular structures, conformations and assemblies in solution. *Q. Rev. Biophys.* 40:191–285.
16. Johs, A., L. Liang, …, W. Wang. 2009. Application of neutron reflectivity for studies of biomolecular structures and functions at interfaces. *In* Neutron Applications in Earth, Energy and Environmental Sciences. L. Liang, R. Rinaldi, and H. Schober, editors. Springer, US, New York. 463–489.

17. Wang, Z., C. Liu, …, L. Shi. 2008. Kinetics of reduction of Fe(III) complexes by outer membrane cytochromes MtrC and OmcA of *Shewanella oneidensis* MR-1. *Appl. Environ. Microbiol.* 74:6746–6755.

18. Myers, C. R., and J. M. Myers. 2004. The outer membrane cytochromes of *Shewanella oneidensis* MR-1 are lipoproteins. *Lett. Appl. Microbiol.* 39:466–470.

19. Shi, L., J. T. Lin, …, B. S. Hooker. 2005. Overexpression of multi-heme C-type cytochromes. *Biotechniques.* 38:297–299.

20. Shi, L., B. Chen, …, T. C. Squier. 2006. Isolation of a high-affinity functional protein complex between OmcA and MtrC: two outer membrane decaheme *c*-type cytochromes of *Shewanella oneidensis* MR-1. *J. Bacteriol.* 188:4705–4714.

21. Konarev, P. V., M. V. Petoukhov, …, D. I. Svergun. 2006. ATSAS 2.1, a program package for small-angle scattering data analysis. *J. Appl. Cryst.* 39:277–286.

22. Guinier, A., and G. Fournet. 1955. Small Angle Scattering of X-Rays. Wiley, New York.

23. Svergun, D. I. 1992. Determination of the regularization parameter in indirect-transform methods using perceptual criteria. *J. Appl. Cryst.* 25:495–503.

24. Svergun, D. I., M. V. Petoukhov, and M. H. J. Koch. 2001. Determination of domain structure of proteins from X-ray solution scattering. *Biophys. J.* 80:2946–2953.

25. Petoukhov, M. V., and D. I. Svergun. 2003. New methods for domain structure determination of proteins from solution scattering data. *J. Appl. Cryst.* 36:540–544.

26. Kozin, M. B., and D. I. Svergun. 2001. Automated matching of high- and low-resolution structural models. *J. Appl. Cryst.* 34:33–41.

27. Volkov, V. V., and D. I. Svergun. 2003. Uniqueness of ab initio shape determination in small-angle scattering. *J. Appl. Cryst.* 36:860–864.

28. Wriggers, W., and P. Chacon. 2001. Using Situs for the registration of protein structures with low-resolution bead models from X-ray solution scattering. *J. Appl. Cryst.* 34:773–776.

29. Humphrey, W., A. Dalke, and K. Schulten. 1996. VMD: visual molecular dynamics. *J. Mol. Graph.* 14:33–38, 27–28.

30. Lide, D. R., editor. 2009. CRC Handbook of Chemistry and Physics. CRC Press/Taylor and Francis, Boca Raton, FL.

31. Covington, A. K., M. Paabo, …, R. G. Bates. 1968. Use of glass electrode in deuterium oxide and relation between standardized pD (paD) scale and operational pH in heavy water. *Anal. Chem.* 40:700–706.

32. Penfold, J., R. M. Richardson, …, J. W. White. 1997. Recent advances in the study of chemical surfaces and interfaces by specular neutron reflection. *J. Chem. Soc., Faraday Trans.* 93:3899–3917.

33. Parratt, L. G. 1954. Surface studies of solids by total reflection of x-rays. *Phys. Rev.* 95:359–369.

34. Nevot, L., and P. Croce. 1980. Characterization of surfaces by grazing x-ray reflection—application to study of polishing of some silicate-glasses. *Rev. Phys. Appl.* 15:761–779.

35. Ankner, J. F., and C. F. Majkrzak. 1992. Subsurface profile refinement for neutron specular reflectivity. *Neutron Opt. Devices Appl.* 1738: 260–269.

36. Glatter, O., and O. Kratky. 1982. Small Angle X-Ray Scattering. Academic Press, London.

37. Myers, J. M., and C. R. Myers. 1998. Isolation and sequence of omcA, a gene encoding a decaheme outer membrane cytochrome *c* of *Shewanella putrefaciens* MR-1, and detection of omcA homologs in other strains of *S. putrefaciens*. *Biochim. Biophys. Acta.* 1373:237–251.

38. Harpaz, Y., M. Gerstein, and C. Chothia. 1994. Volume changes on protein folding. *Structure.* 2:641–649.

39. Umhau, S., G. Fritz, …, P. M. Kroneck. 2001. Three-dimensional structure of the nonaheme cytochrome c from *Desulfovibrio desulfuricans* Essex in the Fe(III) state at 1.89 A resolution. *Biochemistry.* 40:1308–1316.

40. Mylonas, E., and D. I. Svergun. 2007. Accuracy of molecular mass determination of proteins in solution by small-angle X-ray scattering. *J. Appl. Cryst.* 40:S245–S249.

41. Natalello, A., S. M. Doglia, …, R. Grandori. 2007. Role of flavin mononucleotide in the thermostability and oligomerization of *Escherichia coli* stress-defense protein WrbA. *Biochemistry.* 46:543–553.

42. Schlessinger, J. 2000. Cell signaling by receptor tyrosine kinases. *Cell.* 103:211–225.

43. Lies, D. P., M. E. Hernandez, …, D. K. Newman. 2005. *Shewanella oneidensis* MR-1 uses overlapping pathways for iron reduction at a distance and by direct contact under conditions relevant for biofilms. *Appl. Environ. Microbiol.* 71:4414–4426.

44. Schröder, I., E. Johnson, and S. de Vries. 2003. Microbial ferric iron reductases. *FEMS Microbiol. Rev.* 27:427–447.

45. Jacrot, B. 1976. Study of biological structures by neutron-scattering from solution. *Rep. Prog. Phys.* 39:911–953.

46. Quillin, M. L., and B. W. Matthews. 2000. Accurate calculation of the density of proteins. *Acta Crystallogr.* 56:791–794.

47. Lower, B. H., R. D. Lins, …, S. K. Lower. 2008. In vitro evolution of a peptide with a hematite binding motif that may constitute a natural metal-oxide binding archetype. *Environ. Sci. Technol.* 42:3821–3827.